IEEE Access
Multidisciplinary ⋮ Rapid Review ⋮ Open Access Journal

Received 23 June 2023, accepted 14 July 2023, date of publication 20 July 2023, date of current version 28 July 2023.

Digital Object Identifier 10.1109/ACCESS.2023.3297505

RESEARCH ARTICLE

Introduction of Double-Stator Synchronous Reluctance Motor and Modeling

AMIN MAHMOUDI[1], (Senior Member, IEEE), EMAD ROSHANDEL[1], (Member, IEEE), SOLMAZ KAHOURZADE[2], (Member, IEEE), AND WEN L. SOONG[3], (Senior Member, IEEE)

[1]College of Science and Engineering, Flinders University, Adelaide, SA 5042, Australia
[2]STEM, University of South Australia, Adelaide, SA 5000, Australia
[3]School of Electrical and Electronic Engineering, The University of Adelaide, Adelaide, SA 5005, Australia

Corresponding author: Emad Roshandel (emad.roshandel@flinders.edu.au)

ABSTRACT This paper introduces a double-stator synchronous reluctance motor (DS-SynRM) as a solution for reducing the torque ripple of single-stator synchronous reluctance motors (SS-SynRMs). To speed up the design and performance parameter prediction of the DS-SynRM, a magnetic equivalent circuit (MEC) is proposed. To ensure accurate performance prediction of the motor designs using the MEC, a saturation factor is considered in the proposed MEC based on finite element analysis (FEA) results. The accuracy of the developed MEC is validated using 2-D FEA results. A design algorithm based on the proposed MEC in the *dq* reference frame is introduced. The study investigates four different DS-SynRM designs with similar volume based on the proposed design algorithm. The performance parameters of the proposed designs are compared with a conventional SS-SynRM and two previously introduced single-stator SynRMs constructed by expensive materials (i.e., dual phase materials). The simulation results demonstrate the capability of the DS-SynRM in production of a similar torque compared to the SS-SynRM. It is shown that the proper adjustment of the second stator location produces a lower torque ripple using the DS-SynRM topology.

INDEX TERMS Double-stator SynRM, high-power density, high-torque density, magnetic equivalent circuit, synchronous-reluctance motor.

I. INTRODUCTION

Permanent magnet (PM) motors are currently one of the most common type of motors for high-torque applications such as electric vehicles and conveyors [1], [2]. However, they suffer from two main drawbacks: high price and possibility of demagnetization [3]. Synchronous-reluctance motors (SynRMs) are proposed as an alternative for PM machines in industrial applications [4], [5].

Although SynRMs are low-cost and robust, they generally suffer from a relatively low power density (0.1-0.2 kW/kg), high torque ripple (30%-70%), and low power factor (0.5-0.7) [6]. The most promising way of increasing the torque density in SynRMs is the placement of PMs into the rotor flux-barriers, which results in a PM-assisted SynRM [7]. The use of PM in SynRMs compensates the low power factor of SynRMs but for rare-earth magnets this significantly increases the cost. The low power factor of SynRMs increases the power rating of the required inverter [8]. Compared to the NdFeB magnets that are usually used in permanent-magnet synchronous machines (PMSM), ferrite PMs have a lower cost which results in a cheaper synchronous machine [9]. However, these PMs are prone to demagnetization under the strong magnetic fields associated with short-circuit or overload conditions which may occur in real-life operation [10].

Reddy et al. introduced the idea of using dual-phase (DP) materials in the structure of SynRMs [11]. DP materials allow the magnetic permeability of the lamination material to be changed from acting as a ferromagnetic material to a diamagnetic material at different locations in a single lamination. This feature allows the rotor ribs to benefit from diamagnetic characteristics which leads to a better performance in the constant-torque region (about 7% higher torque in this region) as well as a significant performance improvement in the constant-power region (about 300% increase in power at the

The associate editor coordinating the review of this manuscript and approving it for publication was Xiaodong Liang.

maximum speed) [11]. Disadvantages of this material are the high cost and the necessity of a special manufacturing process.

In [12], the authors proposed a SynRM using high-quality cold-rolled grain-oriented electrical steel to reduce the magnetic permeability of the rotor ribs while the torque ripple of the machine is reduced by a special rotor slot pitch angle design. Although reducing the rib flux leads to higher torque density, it offers only limited torque improvements. The ribs tend to saturate and therefore their adverse effect on the performance of the machine is marginal.

Although using a two-stator structure is a well-studied concept for PM motors [13], switched reluctance motors (SRMs) [14], and axial-flux motors [15], it has not been reported for SynRMs. In the double-stator structure, the torque-producing surface of the machine (i.e., the airgap) is increased to enhance the torque density. Such a structure may result in a larger torque ripple in comparison to a single-stator SRM [16]. However, a recent comparative study [17] shows that the torque ripple of a double-stator PM-assisted SynRM machine can be lower than the single-stator design.

Although some types of double-stator machines have been studied previously in [13], [14], [15], [16], and [17], the detailed construction information and design formulas were not reported.

This paper introduces a double-stator design for the SynRM which has not been previously studied in the literature. Figure 1 shows the 2-D view of the cross section of the proposed double-stator motor. In the proposed double-stator structure, the inner stator is surrounded by the rotor. The proposed double-stator synchronous reluctance motor (DS-SynRM) has a comparable power density (about 2.5kW/liter) with published single-stator SynRM motors [11] and [12] while using lower cost materials.

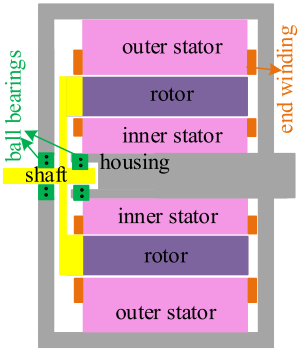

FIGURE 1. Proposed mechanical design of the double-stator SynRM.

Finite-element analysis (FEA) is accurate but is not a computationally-efficient technique for the optimal design of electric machines. A magnetic equivalent circuit (MEC) model with an acceptable accuracy can be a suitable substitute for FEA when an optimization study is needed [18]. Despite previous work on a magnetic equivalent circuit-based (MEC-based) design procedure for the single-stator SynRM (SS-SynRM) [19], there is no published work for the double-stator SynRM using MEC. This paper develops a MEC-based design for the DS-SynRM using the design strategy for SS-SynRM in [19]. The accuracy of the proposed MEC-based model is improved by the consideration of a saturation factor for the proposed model.

The proposed DS-SynRM structure uses the available space between the shaft and airgap of the SS-SynRM to accommodate the second stator. Therefore, the material cost of the DS-SynRM and SS-SynRM is similar. The DS-SynRM manufacturing cost is higher than the SS-SynRMs however the double stator topology allows reducing the torque ripple in SynRMs via appropriate alignment of the stators.

The proposed design method is largely based on the estimation of d- and q-axes inductances of the machine using the MEC. This method not only considers the effect of the number of barriers and their shape, but also investigates different parameters such as flux leakage and iron saturation. In this study, finite-element analysis (FEA) is utilized to improve the accuracy of the MEC simulations.

A comprehensive study is conducted to demonstrate the superior performance of the DS-SynRM against the SS-SynRMs. Various designs of the DS-SynRMs are studied to show the accuracy of the proposed approach in the estimation of the machine performance parameters. The proposed design offers a comparable torque density and power factor with the SS-SynRMs. Considering the low torque ripple of DS-SynRMs, they are promising for application in transport electrification.

II. THEORETICAL FRAMEWORK

The MEC-based design which comes from the estimation of reluctances has been a widely-used method to design single-stator SynRMs [19]. The proposed MEC model uses the MEC equations of the SS-SynRM available in [19]. MEC methods allow more rapid analysis of the electric machines than finite element analysis (FEA) and are generally better suited to optimization studies.

Figure 2 shows 2-D and exploded views of a conventional SS-SynRM and the proposed DS-SynRM. The design parameters of Figure 2(a) determine the MEC model and are used to estimate the reluctance and MEC parameters of the proposed DS-SynRM of Figure 2(c). Figures 2(b) and (d) illustrate the exploded views of a single- and double- stator SynRM structures, respectively.

Figure 3 shows the developed MEC of the double-stator SynRM. The highlighted sections illustrate the MEC of a conventional SS-SynRM. The second stator MEC is added to the d-q axes MEC of the SS-SynRM.

The second stator increases the stator's specific electric loading, which leads to higher electromagnetic torque in comparison to a single-stator SynRM with the same volume [20].

The design procedure considers the MEC of the machine to determine the dimensions. The MEC is faster than the FEA which leads to an increase of the design speed. Therefore, the

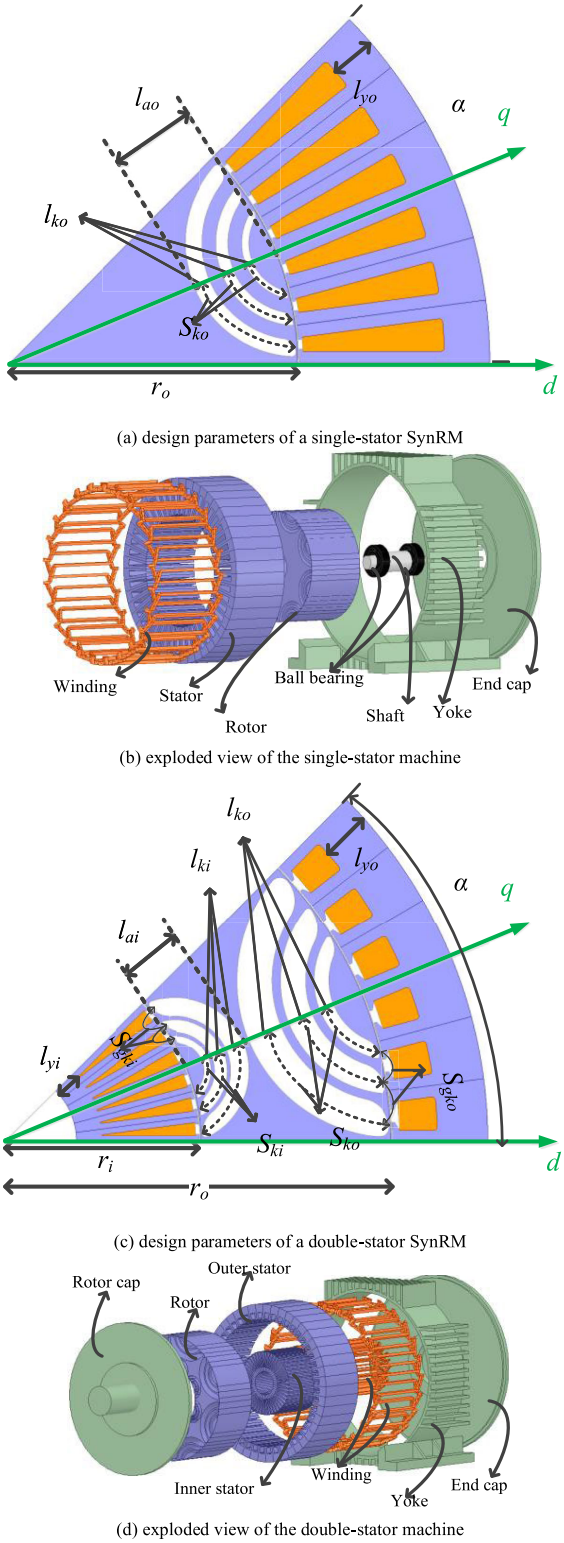

FIGURE 2. 2-D cross-section and 3D exploded views of the single-stator and double-stator SynRMs, α: total arc of a pole (rad); l_{ai}: total thickness of the inner barriers; l_{ao}: total thickness of the outer barriers; l_{ki}: thickness of each barrier near the inner stator; l_{ko}: thickness of each barrier near the outer stator; l_{yi}: yoke thickness of the inner stator; l_{yo}: yoke thickness of the outer stator; r_i: inner airgap radius; r_o: outer airgap radius; S_{ki}: width of each barrier near the inner stator; S_{ko}: width of each barrier near the outer stator. length of k^{th} segments of the rotor barriers near the inner and outer stators are shown by S_{gki} and S_{gko}.

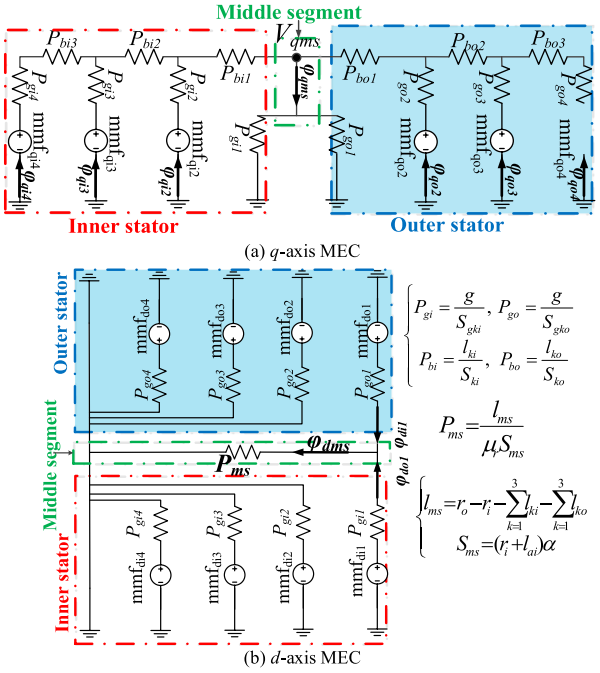

FIGURE 3. MEC of the proposed double-stator SynRM; mmf_q and mmf_d show equivalent magnetic motive force (mmf) of the stator windings along the q- and d-axis; φ_{dms} and φ_{qms} are the magnetic fluxes along d-axis and q-axis; φ_{dk}s and φ_{qk}s show the per-unit values of d- or q- axis airgap fluxes which goes through the related branch of the rotor; V_{qms}: magnetic potential along the q-axis; g: length of the inner and outer airgaps; l_{ms}: the length of the middle tangential segment. S_{ms}: the width of the middle tangential segment; P_g,P_b, and P_{ms} are the per-unit values of airgap, barriers, and middle segment reluctances.

d-q axis reluctances are required to complete the magnetic equivalent circuit of the double-stator SynRM. In the proposed MEC, a number of reluctances are considered to increase the model accuracy. As shown in Figure 2, the barrier reluctances are along the q-axis and the available airgap between the rotor near the inner and outer stators are the only reluctances of the machine along with d-axis. R_{gi} and R_{go} are the airgap reluctances in front of each segment while R_{bi} and R_{bo} are the barrier reluctances in the proposed double-stator MEC. These reluctances are calculated as follow:

$$\begin{cases} R_{gi} = \dfrac{g}{\mu_0 A_{gki}}, & R_{go} = \dfrac{g}{\mu_0 A_{gko}} \\ R_{bi} = \dfrac{l_{ki}}{\mu_0 A_{ki}}, & R_{bo} = \dfrac{l_{ko}}{\mu_0 A_{ko}} \end{cases} \tag{1}$$

The reluctance of the middle tangential segment (R_{ms}) is calculated by (2), where A_{ms} shows the area of the middle tangential segment.

$$R_{ms} = \frac{l_{ms}}{\mu_0 \mu_r A_{ms}} \tag{2}$$

The inner and outer stator radii (r_i and r_o) are required to calculate the end surface of the k^{th} segment of the rotor barriers near the inner and outer stators (A_{gk}) and the surface of the layer near the inner and outer stators (A_k). Using a constant stack length enables per unitizing the permeances by this value. Thus, per-unit permeances are defined where

the barrier lengths are used in the denominator instead of the surface area.

The numbered indices in the MEC in Figure 3, indicate the segments and barriers from the largest to the smallest where i and o indices indicate the inner and outer stators. Using the MEC help simplify the model analysis and allows finding the d-q axes mmfs using the staircase function [19]. The staircase function uses the machine geometry to find the average mmf of each segment when the current is along the q-axis (f_k). If the rated magnetic flux density of B_{fe} is imposed on the motor iron, the magnetic loading factor is calculated as below:

$$b = B_d / B_{fe} \tag{3}$$

where B_d is the peak of the fundamental of the airgap flux density. Note that 1.5T is assumed for B_{fe} in this paper because this is the start of the saturation region for most of commercial lamination materials. The ratio of the magnetic flux densities defined by (3) is the per-unit value for flux density which is required for calculation of the d-axis current and flux linkage. It is reasonable to assume a sinusoidal flux density in the airgap for a well-designed machine.

III. DESIGN OF THE PROPOSED DOUBLE-STATOR SYNRM

The design process and the developed MEC for the DS-SynRM is similar to the SS-SynRM. According to Figure 3, the MEC for the outer and inner stators are the same and the difference is in the dimensions. The windings of the inner and outer stators are connected in series with each other. Thus, the obtained inductances from the MEC for each stator are summed.

To find the main dimensions of the double-stator SynRM design, the following assumptions are made:

- The number of inner and outer stator slots are equal.
- The average magnetic flux densities of the inner and outer airgaps are equal. It means that the total magnetic flux and yoke thickness (l_{yi}) and tooth height (l_{ti}) of the inner stator are proportional to the outer stator's yoke thickness (l_{yo}) and tooth height (l_{to}) times the ratio of outer to inner airgap radius shown in (4) and (5).

$$l_{yi} = \frac{r_i}{r_o}\left(l_{yo}\right) \tag{4}$$

$$l_{ti} = \frac{r_i}{r_o}\left(l_{to}\right) \tag{5}$$

- The equality of the average magnetic flux density in the tooth allows to calculate the inner stator tooth width (w_{ti}) based on the outer stator tooth width (w_{to}) as follows:

$$w_{ti} = \frac{r_i}{r_o}\left(w_{to}\right) \tag{6}$$

- Both stators have similar electrical loading. This requires the slot areas of the outer (A_{sloto}) and inner (A_{sloti}) stators to be proportional to their respective airgap radii.

$$A_{sloti} = \frac{r_i}{r_o}\left(A_{sloto}\right) \tag{7}$$

- The current densities of the inner and outer stators are equal.

One of the important factors in the design of the SynRM is the ratio of the rotor's air and iron (k_{ai}). The role of k_{ai} is the determination of the amount of rotor's air as written in (8).

$$2R_{sh} + 2l_{yi} + 2l_{yo} + l_{ai}(1 + k_{ai}) + l_{ao}(1 + k_{ai}) + 2l_{ti} + 2l_{to} = 2R_s \tag{8}$$

Table 1 lists the design equations of the proposed DS-SynRM. As shown in Figure 3, these equations are similar to the SS-SynRM from the MEC point of view. So, it is only required to use the inner stator relevant dimensions to find the inductances from the MEC.

TABLE 1. Design equations of the proposed double-stator SynRM.

Formulas	
$l_{yo} = (2r_o/P)b$	(9)
$x_{DS} = (r_o - r_i)/(r_o + l_{to} + l_{yo})$	(10)
$w_{to} = (2\pi r_o/N_{slot})bk_t$	(11)
$N_{so} = \frac{\sqrt{2}E}{\omega_s k_w l_{eff} \tau_p \alpha_i B_{ag} b}, N_{si} = N_{so}(\frac{r_i}{r_o}), \alpha_i = \left(\frac{2}{\pi}\right)$	(12)
$L_d = L_{md} + L_s$ $L_q = \underbrace{L_{cq} + L_{fq}}_{Lmq} + L_s$	(13)
$\begin{cases} L_{mdo} = (2r_o l_{stk} N_{so}^2 k_w k_s)/(P^2 k_c g) \\ L_{mdi} = (2r_i l_{stk} N_{si}^2 k_w k_s)/(P^2 k_c g) \end{cases} \rightarrow L_{md} = L_{mdo} + L_{mdi}$	(14)
$\begin{cases} \frac{L_{fqo}}{L_{mdo}} = (4/\pi)(Pk_c g/r_o)\sum_k \frac{l_{ko}}{s_{ko}}\Delta f_k^2 \\ \frac{L_{fqi}}{L_{mdi}} = (4/\pi)(Pk_c g/r_i)\sum_k \frac{l_{ki}}{s_{ki}}\Delta f_k^2 \end{cases} \rightarrow L_{fq} = L_{fqo} + L_{fqi}$	(15)
$\frac{L_{cq}}{L_{mdo}} = 1 - \frac{4}{\pi}\sum_k f_k^2 \Delta\alpha_k$	
$i_d = (P/\sqrt{3}N_{so})(k_c g/k_s \mu_0)B_{fe} b$	(16)

To simplify the rotor design, it is assumed that the reluctance of the barriers is constant. This leads to choosing the thickness of each barrier proportional to its width while an equal thickness of iron segments is considered.

In the SS-SynRM design, the ratio of rotor and stator radii (x_{SS}), which is called the rotor/stator split ratio, is used as a variable to achieve different torques and power factors.

To compare the performance of the double-stator machine with the single-stator SynRM, equation (10) is used to calculate its rotor/stator split ratio. Note that the variation of the rotor air to iron ratio (k_{ai}) results in different values of r_i, r_o, l_{to}, and l_{yo} and hence x_{DS}.

According to (9) and (11), the value of magnetic loading defined by (3) is needed to determine the yoke and tooth thicknesses. In these equations, P is the number of pole pairs. The stator tooth thickness (w_t) is calculated using a similar method in which k_t is the ratio between magnetic flux densities of the tooth and yoke, and N_{slot} represents the number of slots of the machine (11). According to (12), the stack length (l_{stk}), pole pitch (τ_p), flux density in the airgaps (B_{ag}), and

winding factor (k_w) are other important parameters to obtain the stator inner and outer number of turns (N_{si} and N_{so}); where the arithmetic average of the flux density coefficient for a sinusoidal flux density (α_i) is calculated by (12) [21]. The inner and outer windings are connected in series and the number of turns in the inner stator is chosen to give a similar current density to the outer stator.

In summary, the dimensions of the machine are obtained as follows: a constant value is chosen for N_{slot}. In this paper, the N_{slot} is selected base on a reference design [22]. The stator tooth flux density is assumed to be the same as the stator yoke flux density, and hence the ratio k_t is set equal to one. The regular staircase function introduced in [23] is used to find the average and fundamental harmonic magnitude of the airgap flux density. The values are used to find the b, l_{yo}, and w_{to} using (3), (9), and (11), respectively. This information enables calculation of the inner stator dimensions based on (4) to (8). Equations (25) to (35) from [24] are then utilized to find the dimensions of the rotor ribs.

To predict the performance of SynRMs, it is necessary to calculate the motor d- and q-axis inductances. These inductances are found by (13). The portion of the inductances which closes its path through the rotor is shown using the m index; L_{cq} is a portion of the q-axis inductance which represents the flux circulating across each segment; L_{fq} is the portion representing the flux passing between the segments through barriers. The required L_{cq} and L_{fq} are found using (14) and (15).

Ampère's circuital law is used to calculate the magnetizing inductance by (14). To calculate the L_{md}, it is assumed that the airgap flux density is sinusoidal. Thus, the Carter factor (k_c) [25] is used to find L_{mdo} and L_{mdi}. Since the d-axis magnetizing inductance is prone to significant saturation, a saturation factor of k_s is introduced and calculated using FEA to increase the accuracy of the modeling.

This factor is less than or equal to one and is the ratio of the d-axis inductance computed using FEA during operation at rated current over the calculated value by (16) when $k_s = 1$. If the saturation effect is ignored, an error of up to 50% may be observed in the analytical calculation of the inductance and torque.

The saturation factor determination affects the accuracy of the prediction of the torque and power factor. Figure 4 shows the significance of the saturation factor in prediction of the d- and q- axes flux linkages. As shown in (14) and (15), both the d- and q-axis inductances are functions of saturation factor (as they are both functions of L_{md} (14) [19]). The saturation factor helps to determine the q-axis flux required for performance prediction of the machine.

The d-axis inductance does not change with the variation of the size of barriers. Thus, a set of 2-D FEA analyses with ten different d-axis flux paths is executed and for each d-axis flux path, the d-axis inductance is recorded when the maximum flux density in the d-axis path is 2.2 T. The selected steel type (i.e., 35JN300) is fully saturated at this flux density. The calculated d-axis inductance is calculated by (14) for

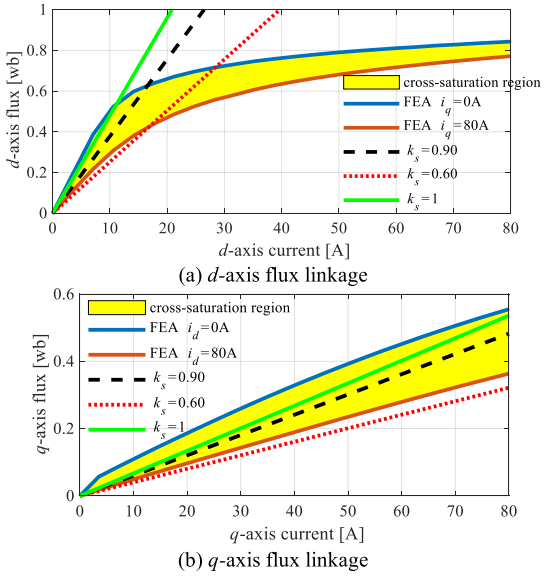

FIGURE 4. The comparison of the effect the saturation factor in the prediction of the flux linkage with the 2-D FEA.

four different magnetic loadings (b) in ten different values of x_{DS}. The corresponding d-axis inductance for considered pair of b and x_{DS} is obtained from 2-D FEA and divided by each analytically calculated inductance. The average of the highest saturation levels (minimum obtained ratio) in each magnetic loading is defined as the saturation factor. This process is executed one time for any geometry as long as the rotor radius, airgap length, and stator slot number are constant.

The calculated average mmf of each segment using the staircase function (f_k) is equal to the q-axis mmfs of each branch in per-unit, which is shown in the MEC (Figure 3(a)). Therefore, the flux passing through each branch can be calculated based on the mmf loop. The calculated flux of each branch is used to obtain the q-axis inductance by (15) [19]. In (15), α_k is the electrical angle of the middle point of each barrier from the rotor d-axis. Consideration of (15) results in the following formulas for calculation of the d-axis inductances of the inner and outer stators:

$$(L_{so}/L_{mdo}) = (4/\pi)(Pk_c g/2r_o)P_{so}\sum_k \Delta f_k^2 \tag{17}$$

$$(L_{si}/L_{mdi}) = (4/\pi)(Pk_c g/2r_i)P_{si}\sum_k \Delta f_k^2 \tag{18}$$

where P_{so} and P_{si} are two constant values which depend on the stator slot dimensions as described in [19].

The q-axis current is obtained from the knowledge of the d-axis current ($i_q = \sqrt{i_0^2 - i_d^2}$), and the maximum current (i_0) based on the thermal capacity of the motor [19].

$$i_0 = \sqrt{k_j k_{fill}\left(\frac{A_{sloto}}{3N_{so}\rho(l_{stk} + l_{ew})}\right)} \tag{19}$$

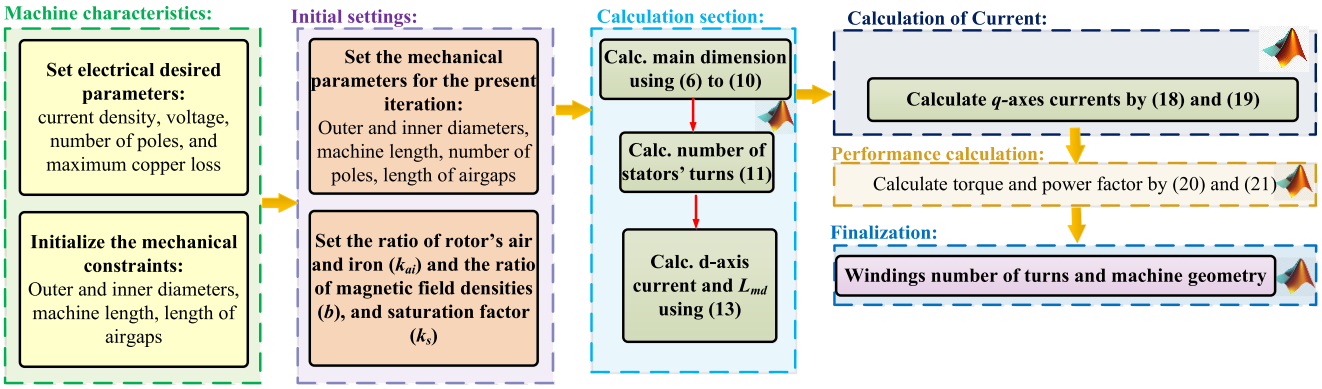

FIGURE 5. The proposed design approach of the studied double-stator SynRM using MEC considering saturation. The saturation factor in this study is equal to 0.6 which is selected based on the explained procedure for calculation of saturation factor (use of initial 2-D FEA results for different d-axis flux path). The considered kai range is 0.7 to 1.5 in this study.

According to (19), the rated current is a function of the number of turns N_{so}, A_{sloto}, l_{stk}, end winding length (l_{ew}), copper resistivity (ρ), and the loss factor (k_j). The aim of the consideration of the loss factor is to apply the maximum permitted loss constraint to the current calculation. If the maximum copper loss per outer stack ratio over the outer stack surface area is shown by LS_{max} then the loss factor is obtained by (20).

$$k_j = 2\pi r_o \times l_{stk} \times LS_{max} \tag{20}$$

As the conductivity of copper varies with the temperature, the simplified analytical model introduced in [26] has been adopted in *Syre* [23] for prediction of the machine average temperature. This model is used to update the copper conductivity in the temperature estimation of the double-stator design.

The calculation of the q-axis current allows finding the electromagnetic torque (τ) and power factor (PF) using the values of L_d and L_q from (21) and (22), respectively.

$$\tau = (3/2)P\left(L_d - L_q\right)\left(i_{do}i_{qo} + i_{di}i_{qi}\right) \tag{21}$$

$$PF = \cos\left(\arctan\left(\frac{R_S(i_{qo}+i_{qi}) + \omega_s L_d(i_{do}+i_{di})}{R_S(i_{do}+i_{di}) - \omega_s L_q(i_{qo}+i_{qi})}\right) - \arctan\left(\frac{(i_{qo}+i_{qi})}{(i_{do}+i_{di})}\right)\right) \tag{22}$$

Some assumptions such as the stack length, inner and outer stator diameters, and number of the poles are required for the design procedure. According to the design flowchart presented in Figure 5, the magnetic loading and ratio of the rotor's air and iron as well as the saturation factor are defined for the given geometry. Determination of these values allows finding the machine barrier sizes and number of turns. The open-source design software *Syre* is used to estimate the mmfs [23]. The stair-case function introduced in *Syre* calculates the average mmf of each segment (f_k) for the calculated d-axis current by (13). The mmf estimations enable calculation of the d- and q-axes inductances by (13) and (15).

TABLE 2. Design specifications and limits.

Parameter	Value
Stator outer diameter [mm]	269.0
Stack length [mm]	83.4
Number of pole pairs	4
Number of stator slots	48
Inner radius of the inner stator [mm]	20.0
Inner and outer airgaps [mm] [27-29]	0.50
Rated phase AC voltage [V]	140
Operating speed [rpm]	750
Copper loss per outer stack surface (LS_{max}) [kW/m^2]	11.5
Permitted current density [A/mm^2]	10
Stator winding slot fill factor [%]	57
Stator winding factor	0.96
Lamination stacking factor	0.95
Lamination material	35JN300

Finally, the q-axis current is found by (18) and used to estimate the torque and power factor using (20) and (21).

IV. DESIGN AND ANALYSIS

In this section, a multi-objective optimization is executed to understand the possible superiority of the DS-SynRM against the SS-SynRM. To analyse the accuracy of the proposed MEC, four designs with significantly different performance parameters are selected in the optimization search space and the performance parameters of each design is compared with the 2-D FEA results. Finally, the performance parameters of the optimized DS-SynRM and SS-SynRM are compared with each other.

The optimization and sensitivity analysis are conducted for the geometry and specifications tabulated in Table 2 which is based on the Toyota Prius' motor geometry, electric loading, and magnetic loading [22]. A single-layer distributed winding is assumed for the design and analysis. It should be noted that the choice of 10A/mm^2 current density necessitates a forced water-cooling system for this machine which is not covered in this paper. According to the explained design procedure,

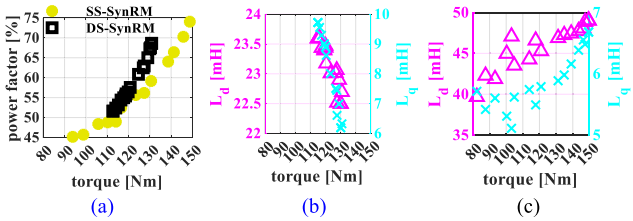

FIGURE 6. (a) The Pareto front of the executed multi-objective optimization on the DS-SynRM and SS-SynRM using the MEC, (b) DS-SynRM design and (c) SS-SynRM design d- and q-axes inductances of the presented points on the Pareto front.

the lamination material, slot fill factor, and the permitted loss per outer stack are the other design requirements as shown in Table 2.

Because the reference Toyota Prius design is an eight-pole machine, this number of poles is selected for analysis and investigation of SynRMs in this paper. It should be noted that the SynRM power factor could be improved by reducing the number of poles because of the increase of the magnetizing inductance.

A. OPTIMIZATION AND SENSITIVITY ANALYSIS

The proposed MEC is used in a multi-objective optimization study. The considered variables of the optimization are the rotor/stator split and the magnetic loading. In a non-saturated SynRM, the d- and q-axis currents are equal (i.e., current angle of 45°) to obtain the maximum torque per ampere (MTPA). The current angle is increased in presence of the iron saturation. Hence, a constant value of 55° is selected as the current angle in the optimization.

In the optimal design of the DS-SynRM, the magnetic loading (b) and x_{DS}, limits for the optimization are 0.4 to 0.6 and 0.3 to 0.45, respectively. The considered ranges of the magnetic loading for the SS-SynRM and DS-SynRM are equal. The range of the variation of the x_{SS} for the SS-SynRM design is 0.5 to 0.7, which is larger as there is more space on the rotor side. A multi-objective problem with the following objective functions is defined:

$$\max\,(power\ factor) \tag{22a}$$

$$\max\,(torque) \tag{22b}$$

According to the considered objective functions, the power factor and torque are maximized to find the Pareto front. The multi-objective genetic algorithm is executed on the defined problems for both the SS-SynRM and DS-SynRM. The results of these optimization studies are presented as two Pareto fronts in Figure 6a and demonstrate the superiority of SS-SynRM topology in generating larger torque compared to the DS-SynRM for a given power factor. It is seen that the torque does not vary much for higher values of power factor. This is mainly because of the saturation of the flux paths on the rotor side. For higher power-factor designs, the d-axis flux paths are narrow leading to the increase of the

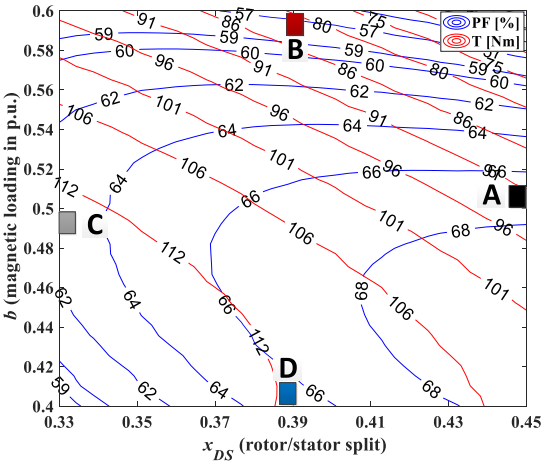

(a) Double-stator SynRM (design A: highest power factor; design B: lowest torque; design C: a midpoint design in terms of torque and power factor; design D: Highest torque).

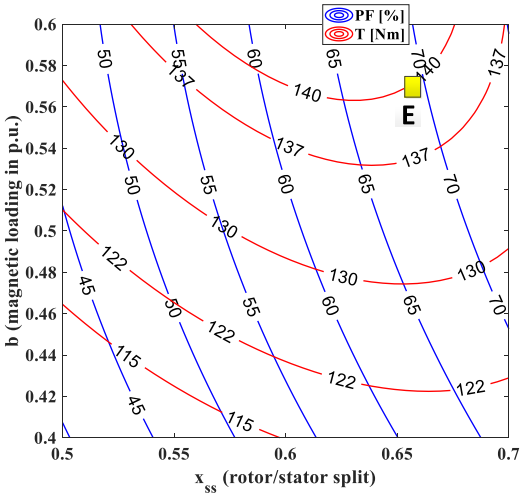

(b) Single stator SynRM (design E: highest torque)

FIGURE 7. Torque and *PF* contours of the studied SynRMs.

saturation which limits the torque increase. The d- and q-axis inductances of designs on the Pareto front are presented in Figures 6b and 6c. As expected, the maximum torque occurs when the difference between the inductances is at its maximum. Also, it is seen that the inductance variation is smaller for the optimal DS-SynRM designs compared to the SS-SynRM. According to Figure 6, the power factor of the DS-SynRM is 68% at 130Nm; while the SS-SynRM maximum torque and power factors are 147Nm and 75%, respectively.

It was found that the optimization algorithm needed to solve about 1,200 different geometries to find the optimum design. The fast speed of the proposed MEC model enables finding the optimal design in about 6 seconds using a desktop computer with 128GB RAM and Core i9-7200X CPU @ 3.3GHz. On the same computer, a 2-D FEA analysis of the design needs about 120 hours to find the optimal design. Therefore, the MEC allows considerable time saving for optimization of the DS-SynRM design.

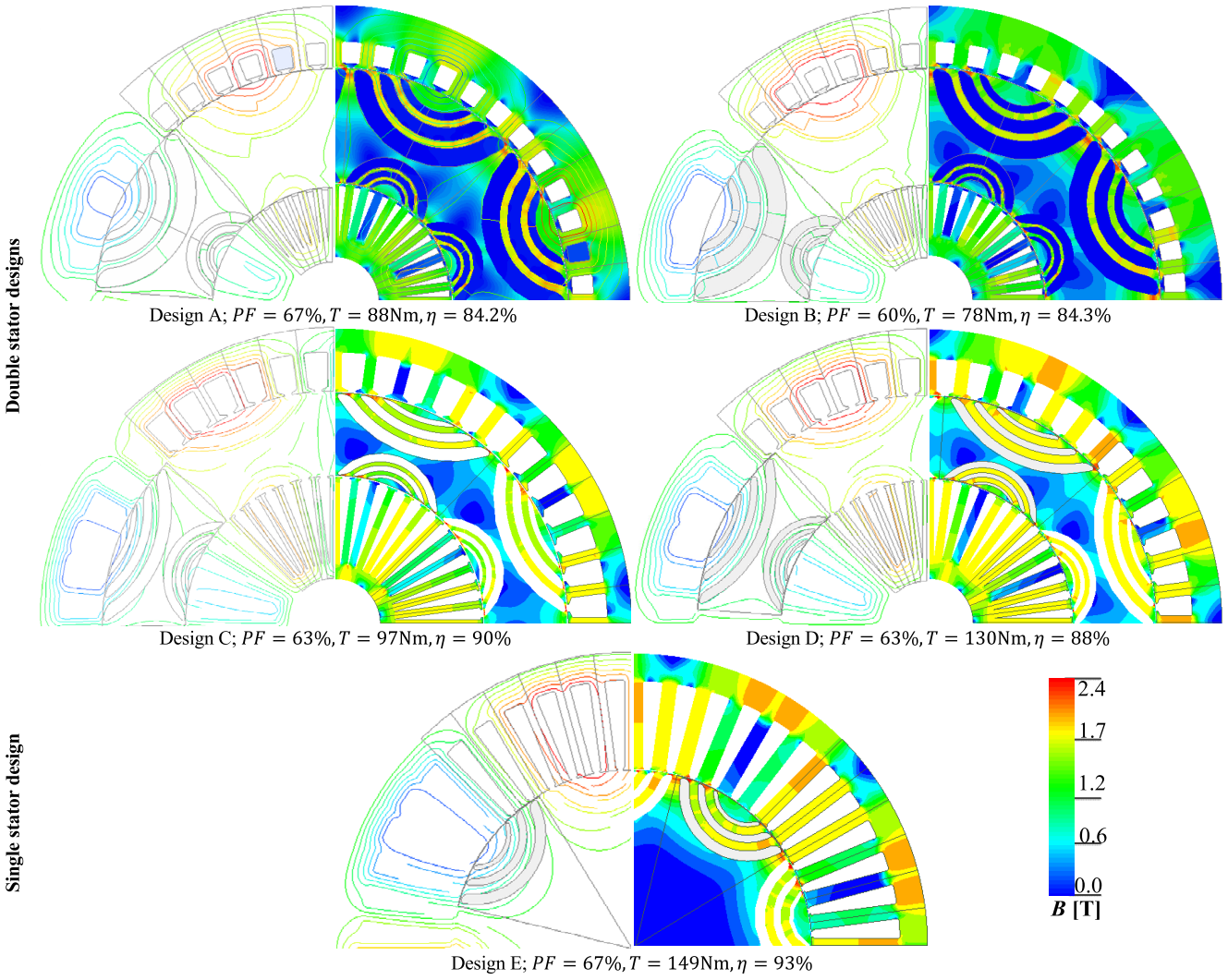

FIGURE 8. Field analysis of the double-stator (A-D) and single-stator SynRMs for further studies. The simulation has been executed when the rated current is injected in the *d*-axis direction and *q*-axis current is zero. The operating speed is 750rpm.

TABLE 3. Comparison of the analytically calculated performance parameters with the 2-D FEA results.

	Design A		Design B		Design C		Design D		Design E	
	T [Nm]	PF [%]	T [Nm]	PF [%]	T [Nm]	PF [%]	T [Nm]	PF [%]	T [Nm]	PF [%]
MEC	91.1	66.7	80.3	57.6	112.6	62.1	111.8	65.3	139	65.1
FEA	88.4	67.3	78.7	60.1	97.8	62.6	130.2	63.4	149	67.1

Table 3 compares the analytically calculated power factor and torque for each considered design with the FEA results. According to this table, the accuracy of the model by consideration of saturation factor of 0.6 shows that the results of MEC is in a good agreement with the FEA results.

Figure 7 shows the contours of torque and power factor when varying b, x_{DS}, and x_{SS} using the proposed MEC at a constant saturation factor of 0.6 for both DS-SynRM and SS-SynRM. As presented in Figure 7a, the rotor/stator split and magnetic loading have a significant role in the variation

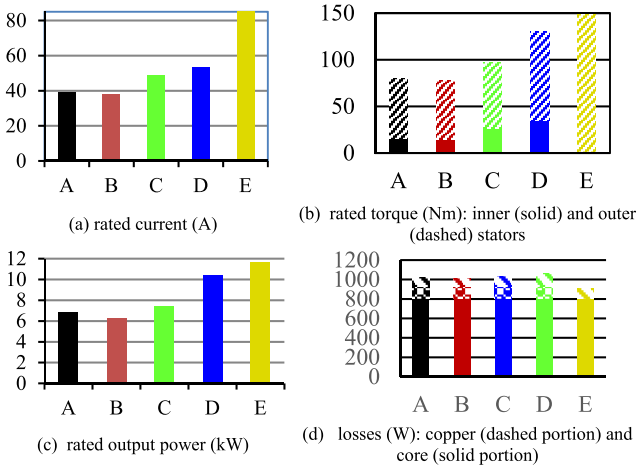

FIGURE 9. 2-D FEA results comparing the rated current, output power, losses and torque of the different designs. The operating speed for the calculations is 750 rpm.

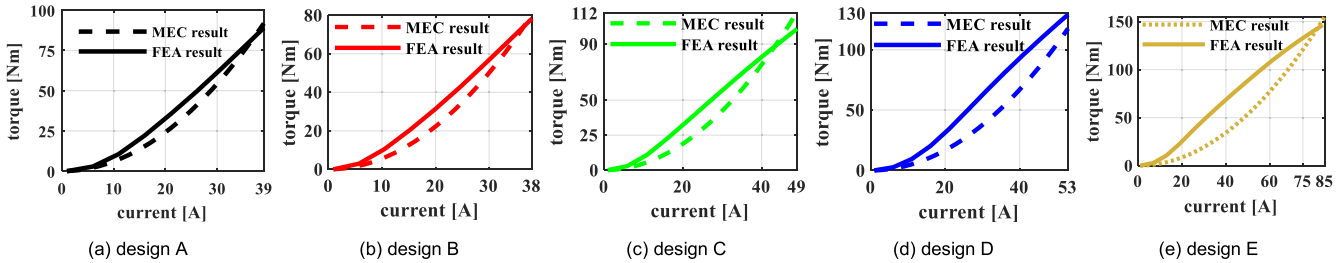

FIGURE 10. Comparison of the MEC model against 2D FEA results in prediction of the MTPA trajectory.

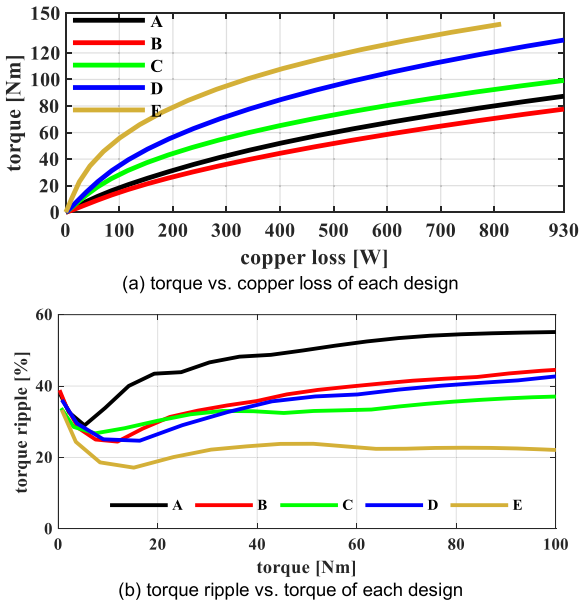

FIGURE 11. FEA results showing (a) torque versus copper loss, and (b) the torque ripple versus average torque of each design.

of the torque and power factor of DS-SynRM. On the other hand, the torque variation in the SS-SynRM has less dependency on the rotor/stator split. Also, the power factor of the SS-SynRM is less affected by variations of the magnetic loading compared to the DS-SynRM.

To assess the accuracy of the developed MEC results, four designs with significantly different values of torque and power factor were selected from Figure 7a (i.e., A, B, C, and D points). In addition, point E is a SS-SynRM design with a high-power factor and torque, and was selected for validation of the SS-SynRM model introduced in [23].

B. DISCUSSION ON DESIGNS

To accurately study the selected designs and validate the analytically calculated features, these designs are simulated using the 2-D Ansys Electromagnetics software package where about 8,000 elements were considered to simulate one pole. A transient FEA is executed to calculate the designed machine's performance parameters. The windings are excited using current sources at the operating speed.

The flux density distribution of the considered designs is presented in Figure 8. The effects of b and k_{ai} variations on the stator cross sections, size of the slots, and shape of

TABLE 4. Performance comparison of the proposed DS-SynRM with the single-stator SynRMs available in the literature.

Parameter \ Design	Proposed DS-SynRM (design D)	Studied SynRM (design E)	SynRM [30]	SynRM [31]
Power	9.44 kW	11.6 kW	5.50 kW	1.20 kW
Torque	130 Nm	149 Nm	60 Nm	7 Nm
Speed	750 rpm	750 rpm	850 rpm	1500 rpm
Power factor	0.64	0.67	--	0.72
Efficiency [%]	88	93	--	86
Current density	10 A/mm^2	10 A/mm^2	--	--
Power density	0.25 kW/kg	0.31 kW/kg	0.27 kW/kg	0.13 kW/kg
Torque density	3.41 Nm/kg	4.01 Nm/kg	2.69 Nm/kg	0.79 Nm/kg

the rotor barriers are observed in this figure. All designs have a relatively high magnetic loading, which shows they are working at their maximum performance. Design D has thinner barriers compared to B and design A has less stator winding area compared to design C.

To compare the performance of the proposed designs with the conventional single-stator SynRM, *Syre* software [23] is used to design a SS-SynRM (design E) in the same volume as the DS-SynRMs (see Figure 8). According to these figures the SS-SynRM offers higher torque and efficiency compared to the proposed double stator designs. It is mainly because of the larger slot area which enables injecting larger current with the same current density as the DS-SynRMs.

Figure 9 shows the rated current, output power, copper loss and core loss corresponding to each design. The comparison shows the SS-SynRM benefits from a larger rated current which leads to the increase of its rated torque and power. The ohmic loss in Design E is also less than the DS-SynRMs which brings about its higher efficiency.

As expected, based on Figure 8, Design D has the highest power and torque among the DS-SynRM designs. Its torque density is 26% higher than the other DS-SynRMs. Due to the smaller airgap volume for the inner stator and smaller slot area of the winding which limits the current, the DS-SynRMs have not offered higher torque compared to the SS-SynRM. The SS-SynRM higher torque density results from its larger rated current (see Figure 9).

The contribution of each stator in torque generation for all designs are shown in Figure 9(b). The electromagnetic torque of the inner stator is lower than the outer stator. However, in designs C and D this accounts for about 27% of the total torque.

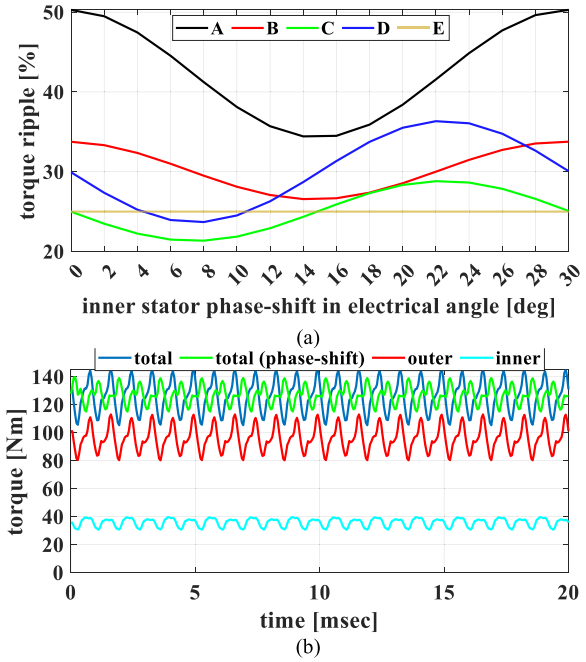

FIGURE 12. 2-D FEA results for the analysis effect of the rotation of second stator for reduction of the torque ripple in the DS-SynRM. (a) the torque ripple variation of different designs. (b) the torque waveforms of Design D to show the effect of the torque ripple reduction.

Figure 10 compares the MTPA points for different current levels calculated by MEC and FEA. The 2-D FEA and proposed MEC results are similar near the rated operating points, as expected since the inductances of the rated point are considered in the saturation model.

The copper loss is proportional to the square of current. As shown in (21), before saturation, the torque also increases with the square of current, however after saturation this relationship is roughly linear (see Figure 10). Based on this, in Figure 11(a) which shows torque versus copper loss, before saturation the torque is proportional to the square root of copper loss, and at larger currents, linearly proportional to copper loss. Figure 11(b), designs C and D have lower torque ripple in comparison to the other double-stator designs at higher torque values. Design D can generate 30 Nm electromagnetic torque more than design C at a current of 50A at the expense of larger torque ripple.

Table 4 compares the performance parameters of the proposed DS-SynRM machine with the SS-SynRM and two other SynRMs from the literature. It demonstrates the comparable torque and power density of the developed DS-SynRM designs compared to the SynRM designs from the literature, despite one of these having twice the rated speed.

C. TORQUE RIPPLE REDUCTION

The literature shows the torque ripple of the SynRMs, is normally in the range of 25% to 60% [5], [9], [31]. Therefore, the studied machines in this paper are within a reasonable range of torque ripple. Skewing can be used to reduce this torque ripple at the cost of some reduction in average torque.

The double-stator design can also be used to reduce the torque ripple of the machine by slight modification to the position of the inner stator compared to the outer stator. This can reduce the main harmonic of the torque ripple. A phase shift which is obtained by rotation of the inner stator is used to decrease the torque ripple.

The torque ripple changes sinusoidally by rotating the second stator under a pole. This effect for the considered case studied is shown in Figure 12a. According to this figure, the torque ripple of the designs C and D can be less than the single stator design with optimum positioning of the second stator. Figure 12b shows the inner, outer, and total wave form torque of the design D and the modified stator version with the minimum torque ripple. This figure demonstrates the effectiveness of the rotation of the second stator to reduce the torque ripple from 35% to 22%.

It should be highlighted that the design process used did not include the optimization of the torque ripple due to the limitations of the proposed MEC for accurate prediction of the torque ripple.

V. CONCLUSION

A double-stator structure of the SS-SynRM was introduced in this paper to investigate its possible advantages. A magnetic equivalent circuit considering the saturation effect was proposed. An accurate estimation of the saturation factor plays an important role in the prediction of the d-axis flux using the proposed analytical design approach. In the considered geometry, ten d-axis flux paths were considered, and their corresponding d-axis inductance were obtained using 2-D FEA analysis. The comparison of the analytically calculated d-axis inductances with the 2-D FEA results showed 0.6 is a proper saturation factor in the given geometry. In the proposed design approach, the performance parameters of the double-stator SynRM was estimated based on the proposed magnetic equivalent circuit. The proposed design approach was validated by finite-element analysis of four different designs. The double-stator machine showed lower torque density and power factor compared to the conventional SS-SynRMs.

The torque ripple analysis was executed to see the effect of the use of double-stator topology on the variation of torque ripple. The initial result showed the DS-SynRMs have 10% to 30% larger torque ripple compared to the SS-SynRM. However, a method was introduced to reduce the torque ripple in presence of the second stator. The result of the analysis showed the torque ripple using the rotation of the second stator can lead to the reduction of torque ripple by 15%. This approach showed it is possible to reach lower torque ripple using the double-stator topology compared to the single-stator design.

Future work to improve the proposed machine's power factor includes improving its saliency ratio, e.g., by optimising the shapes of the rotor flux barriers, and by possibly including non-rare earth magnets in the flux barriers. Other possible subjects for future work are: inclusion of torque ripple in the

objective function for optimization, the thermal and structural analysis of the double-stator design and prototyping of the machine.

ACKNOWLEDGMENT

The authors would like to thank Babak Dianati for his advice on modeling of the studied machines.

REFERENCES

[1] J.-W. Kwon, N. Baloch, and B.-I. Kwon, "High gear ratio flux switching permanent magnet machine for high torque performance," *IEEE Access*, vol. 8, pp. 121630–121636, 2020.

[2] I. Petrov, P. Lindh, M. Niemelä, E. Scherman, and J. Pyrhönen, "High-torque-density IPMSM rotor pole geometry adjustment for smooth torque," *IEEE Access*, vol. 7, pp. 52650–52658, 2019.

[3] K.-Y. Yoon and K.-Y. Hwang, "Optimal design of spoke-type IPM motor allowing irreversible demagnetization to minimize PM weight," *IEEE Access*, vol. 9, pp. 65721–65729, 2021.

[4] N. Bianchi, S. Bolognani, D. Bon, and M. Dai Pre, "Rotor flux-barrier design for torque ripple reduction in synchronous reluctance and PM-assisted synchronous reluctance motors," *IEEE Trans. Ind. Appl.*, vol. 45, no. 3, pp. 921–928, May/Jun. 2009.

[5] M. Alani, M. Degano, N. Bianchi, H. Mahmoud, and C. Gerada, "Analysis and design of dual-rotor synchronous reluctance machine," *IEEE J. Emerg. Sel. Topics Power Electron.*, vol. 9, no. 4, pp. 4376–4383, Aug. 2021, doi: 10.1109/JESTPE.2020.3047404.

[6] Y. Wang, D. Ionel, D. G. Dorrell, and S. Stretz, "Establishing the power factor limitations for synchronous reluctance machines," *IEEE Trans. Magn.*, vol. 51, no. 11, pp. 1–4, Nov. 2015.

[7] M. S. Mirazimi and A. Kiyoumarsi, "Magnetic field analysis of SynRel and PMASynRel machines with hyperbolic flux barriers using conformal mapping," *IEEE Trans. Transport. Electrific.*, vol. 6, no. 1, pp. 52–61, Mar. 2020.

[8] S.-J. Kim, J.-B. Im, S. C. Go, J.-N. Bae, W.-H. Kim, K.-S. Kim, C.-J. Kim, and J. Lee, "Robust torque control of DC link voltage fluctuation for SynRM considering inductances with magnetic saturation," *IEEE Trans. Magn.*, vol. 46, no. 9, pp. 3705–3708, Sep. 2010.

[9] N. Bianchi, S. Bolognani, E. Carraro, M. Castiello, and E. Fornasiero, "Electric vehicle traction based on synchronous reluctance motors," *IEEE Trans. Ind. Appl.*, vol. 52, no. 6, pp. 4762–4769, Nov. 2016.

[10] A. Vagati, B. Boazzo, P. Guglielmi, and G. Pellegrino, "Design of ferrite-assisted synchronous reluctance machines robust toward demagnetization," *IEEE Trans. Ind. Appl.*, vol. 50, no. 3, pp. 1768–1779, May 2014.

[11] P. B. Reddy, A. M. El-Refaie, M. Zou, D. Pan, J. P. Alexander, N. Tapadia, K. Grace, K.-K. Huh, and F. Johnson, "Performance testing and analysis of synchronous reluctance motor utilizing dual-phase magnetic material," *IEEE Trans. Ind. Appl.*, vol. 54, no. 3, pp. 2193–2201, May 2018.

[12] S. Taghavi and P. Pillay, "A novel grain-oriented lamination rotor core assembly for a synchronous reluctance traction motor with a reduced torque ripple algorithm," *IEEE Trans. Ind. Appl.*, vol. 52, no. 5, pp. 3729–3738, Sep. 2016.

[13] J. Zhang, B. Zhang, G. Feng, and B. Gan, "Design and analysis of a low-speed and high-torque dual-stator permanent magnet motor with inner enhanced torque," *IEEE Access*, vol. 8, pp. 182984–182995, 2020.

[14] L. Maharjan, "Comprehensive report on design and development of a 100-kW DSSRM," *IEEE Trans. Transport. Electrific.*, vol. 4, no. 4, pp. 835–856, Dec. 2018.

[15] C. Hong, W. Huang, and Z. Hu, "Design and analysis of a high-speed dual stator slotted solid-rotor axial-flux induction motor," *IEEE Trans. Transport. Electrific.*, vol. 5, no. 1, pp. 71–79, Mar. 2019.

[16] M. Asgar and E. Afjei, "Radial force reduction in a new flat-type double-stator switched reluctance motor," *IEEE Trans. Energy Convers.*, vol. 31, no. 1, pp. 141–149, Mar. 2016.

[17] Y. Zhang, S. Yu, G. Liu, and H. Zhang, "Comparative research for a novel dual-stator synchronous machine with permanent magnet-reluctance composite rotor," *IEEE Trans. Appl. Supercond.*, vol. 30, no. 4, pp. 1–5, Jun. 2020.

[18] A. Mahmoudi, N. A. Rahim, and W. P. Hew, "An analytical complementary FEA tool for optimizing of axial-flux permanent-magnet machines," *Int. J. Appl. Electromagn. Mech.*, vol. 37, no. 1, pp. 19–34, Aug. 2011.

[19] A. Vagati and T. A. Lipo, "Synchronous reluctance motors and drives: A new alternative," in *Proc. IEEE Ind. Appl. Soc. Meeting*, Sep. 1994, pp. 1–304.

[20] C. Röth, F. Milde, D. Trebbels, J. Schmidt, and M. Doppelbauer, "A stator with offset segments and a double stator design for the reduction of torque ripple of a switched reluctance motor," *IEEE Trans. Energy Convers.*, vol. 37, no. 2, pp. 1233–1240, Jun. 2022, doi: 10.1109/TEC.2021.3124011.

[21] J. Pyrhönen, T. Jokinen, and V. Hrabovkowá, *Design of Rotating Electrical Machines*, 2nd ed. Hoboken, NJ, USA: Wiley, 2014.

[22] K. Kiyota and A. Chiba, "Design of switched reluctance motor competitive to 60-kW IPMSM in third-generation hybrid electric vehicle," *IEEE Trans. Ind. Appl.*, vol. 48, no. 6, pp. 2303–2309, Nov. 2012, doi: 10.1109/TIA.2012.2227091.

[23] F. Cupertino and G. Pellegrino. *Syre is Available*. Polytechnic University of Turin. Accessed: Mar. 2, 2023. [Online]. Available: http://sourceforge.net/projects/syr-e/

[24] M. Gamba, G. Pellegrino, E. Armando, and S. Ferrari, "Synchronous reluctance motor with concentrated windings for IE4 efficiency," in *Proc. IEEE Energy Convers. Congr. Expo. (ECCE)*, Oct. 2017, pp. 3905–3912, doi: 10.1109/ECCE.2017.8096686.

[25] A. C. Viorel, I.-A. Viorel, and L. Strete, "On the calculation of the carter factor in the slotted electric machines," in *Proc. Int. Conf. Expo. Electr. Power Eng. (EPE)*, Oct. 2014, pp. 332–336, doi: 10.1109/ICEPE.2014.6969923.

[26] A. Boglietti, A. Cavagnino, M. Lazzari, and M. Pastorelli, "A simplified thermal model for variable-speed self-cooled industrial induction motor," *IEEE Trans. Ind. Appl.*, vol. 39, no. 4, pp. 945–952, Jul. 2003, doi: 10.1109/TIA.2003.814555.

[27] Z. Z. Wu, Z. Q. Zhu, and J. T. Shi, "Novel doubly salient permanent magnet machines with partitioned stator and iron pieces rotor," *IEEE Trans. Magn.*, vol. 51, no. 5, pp. 1–12, May 2015, doi: 10.1109/TMAG.2015.2404826.

[28] D. Kim, H. Hwang, S. Bae, and C. Lee, "Analysis and design of a double-stator flux-switching permanent magnet machine using ferrite magnet in hybrid electric vehicles," *IEEE Trans. Magn.*, vol. 52, no. 7, pp. 1–4, Jul. 2016, doi: 10.1109/TMAG.2016.2532360.

[29] J. Zhao, Y. Wang, J. Li, and H. Hu, "Comparative study on torque performance of five-phase single-stator and double-stator permanent magnet synchronous motors," *CES Trans. Electr. Mach. Syst.*, vol. 6, no. 1, pp. 46–52, Mar. 2022, doi: 10.30941/CESTEMS.2022.00007.

[30] S. S. Maroufian and P. Pillay, "Torque characterization of a synchronous reluctance machine using an analytical model," *IEEE Trans. Transport. Electrific.*, vol. 4, no. 2, pp. 506–516, Jun. 2018.

[31] M. Ferrari, N. Bianchi, A. Doria, and E. Fornasiero, "Design of synchronous reluctance motor for hybrid electric vehicles," *IEEE Trans. Ind. Appl.*, vol. 51, no. 4, pp. 3030–3040, Jul. 2015.

AMIN MAHMOUDI (Senior Member, IEEE) received the B.Sc. degree in electrical engineering from Shiraz University, Shiraz, Iran, in 2005, the M.Sc. degree in electrical power engineering from the Amirkabir University of Technology, Tehran, Iran, in 2008, and the Ph.D. degree from the University of Malaya, Kuala Lumpur, Malaysia, in 2013. He is currently a Senior Lecturer with Flinders University, Adelaide, Australia. He has authored/coauthored over 160 papers in international journals and conferences. His main research interest includes where the electrical energy conversion plays a major role, such as the electrical machines and drives, renewable energy systems, and hybrid power networks. It includes the transportation electrification in which the sustainable energy efficient solutions are realized by advanced electric motors, power electronics, energy management systems and controls for electrified powertrains, and electric vehicles. He is a member of the Engineers Australia (MIEAust) and a Chartered Professional Engineer (C.P.Eng.).

EMAD ROSHANDEL (Member, IEEE) received the B.Sc. degree (Hons.) in electrical engineering from Shiraz University, in 2013, the M.Sc. degree (Hons.) in electrical engineering from the Isfahan University of Technology, in 2016, and the Ph.D. degree in electrical engineering from Flinders University, in 2023.

He was the Research and Development Director of the Power, Electronic, and Control (PEC) Laboratory, Eram Sanat Mooj Gostar Company, Shiraz, Iran, from 2016 to 2020. During his tenure, he played a pivotal role in establishing the development of switching power supplies and motor drives. He was a Researcher with The University of Adelaide, from 2020 to 2023. He was the Principal Researcher and a Developer of switching power supplies for extra low-voltage lighting with MyModular Pty Ltd., from 2021 to 2022. He was the Designer of high-power efficient electric machines with Sovereign Propulsion System Pty Ltd., from 2022 to 2023. He is currently with CPIE pharmacy services, where he leads the research and development efforts in designing the next generation of infusion pumps for medical applications. He is the principal author/coauthor of over 50 journal articles and conference papers.

SOLMAZ KAHOURZADE (Member, IEEE) received the B.S. degree in electrical engineering from the K. N. Toosi University of Technology, Tehran, Iran, the M.Eng. degree from the University of Malaya, Kuala Lumpur, Malaysia, and the Ph.D. degree from The University of Adelaide, Adelaide, SA, Australia. She was a Research Associate and a Lecturer with The University of Adelaide, from 2017 to 2020. She is currently a Lecturer with the University of South Australia. Her research interests include PM and reluctance machines, renewable energy generation, and energy storage in power systems.

WEN L. SOONG (Senior Member, IEEE) was born in Kuala Lumpur, Malaysia. He received the B.Eng. degree in electrical engineering from The University of Adelaide, Adelaide, SA, Australia, in 1989, and the Ph.D. degree in electrical engineering from the University of Glasgow, Glasgow, U.K., in 1993. From 1994 to 1998, he was with General Electric Corporate Research and Development, Schenectady, NY, USA. In 1998, he joined The University of Adelaide. His research interests include PM and reluctance machines, renewable energy generation, and energy storage in power systems.